Vibrational mode analysis and heat capacity calculation of $K_2SiSi_3O_9$-wadeite

Linlin Chang, Xi Liu, Hong Liu, Hiroshi Kojitani & Sicheng Wang

Physics and Chemistry of Minerals

ISSN 0342-1791
Volume 40
Number 7

Phys Chem Minerals (2013) 40:563-574
DOI 10.1007/s00269-013-0593-5

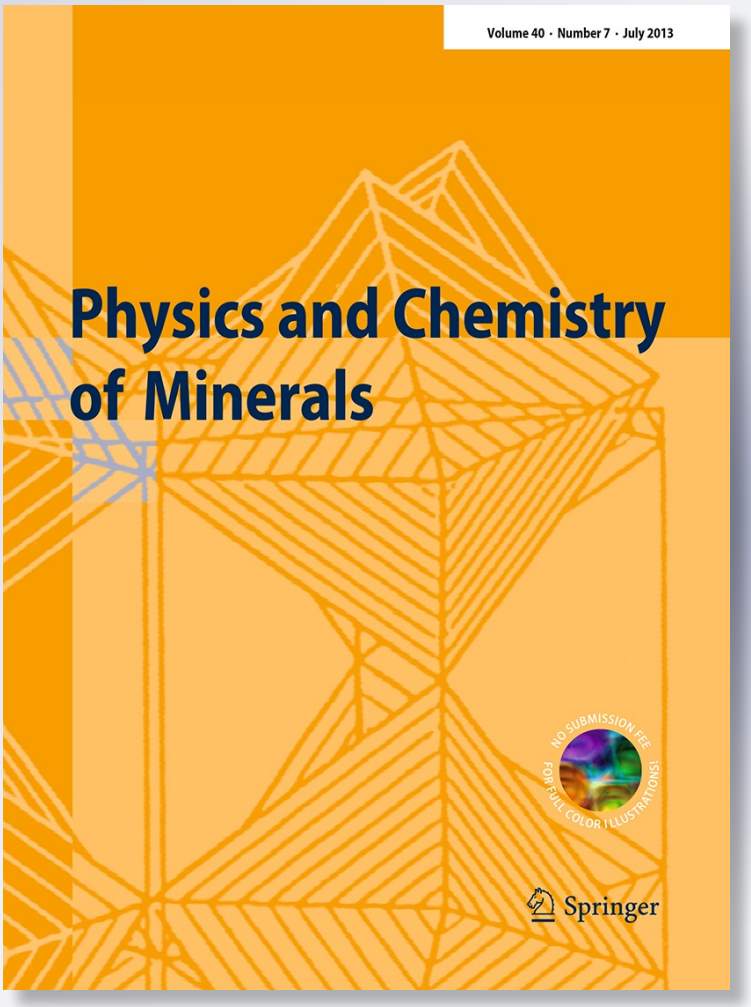

Springer

Phys Chem Minerals (2013) 40:563–574
DOI 10.1007/s00269-013-0593-5

ORIGINAL PAPER

Vibrational mode analysis and heat capacity calculation of $K_2SiSi_3O_9$-wadeite

Linlin Chang · Xi Liu · Hong Liu · Hiroshi Kojitani · Sicheng Wang

Received: 4 February 2013 / Accepted: 17 April 2013 / Published online: 27 April 2013

Abstract The phonon dispersions and vibrational density of state (VDoS) of the $K_2SiSi_3O_9$-wadeite (Wd) have been calculated by the first-principles method using density functional perturbation theory. The vibrational frequencies at the Brillouin zone center are in good correspondence with the Raman and infrared experimental data. The calculated VDoS was then used in conjunction with a quasi-harmonic approximation to compute the isobaric heat capacity (C_P) and vibrational entropy (S^0_{298}), yielding $C_P(T) = 469.4(6) - 2.90(2) \times 10^3\ T^{-0.5} - 9.5(2) \times 10^6\ T^{-2} + 1.36(3) \times 10^9\ T^{-3}$ for the T range of 298–1,000 K and $S^0_{298} = 250.4$ J mol^{-1} K^{-1}. In comparison, these thermodynamic properties were calculated by a second method, the classic Kieffer's lattice vibrational model. On the basis of the vibrational mode analysis facilitated by the first-principles simulation result, we developed a new Kieffer's model for the Wd phase. This new Kieffer's model yielded $C_P(T) = 475.9(6) - 3.15(2) \times 10^3\ T^{-0.5} - 8.8(2) \times 10^6\ T^{-2} + 1.31(3) \times 10^9\ T^{-3}$ for the T range of 298–1,000 K and $S^0_{298} = 249.5(40)$ J mol^{-1} K^{-1}, which are in good agreement both with the results from our first method containing the component of the first-principles calculation and with some calorimetric measurements in the literature.

Keywords First-principles simulation · Heat capacity · Kieffer's lattice vibrational model · $K_2SiSi_3O_9$-wadeite · Vibrational density of states

L. Chang · X. Liu (✉) · S. Wang
Key Laboratory of Orogenic Belts and Crustal Evolution, Ministry of Education of China, Beijing 100871, China
e-mail: xi.liu@pku.edu.cn

L. Chang · X. Liu · S. Wang
School of Earth and Space Sciences, Peking University, Beijing 100871, China

H. Liu
Institute of Earthquake Science, China Earthquake Administration, Beijing 100036, China

H. Kojitani
Department of Chemistry, Gakushuin University, 1-5-1 Mejiro, Toshima-ku, Tokyo 171-8588, Japan

Introduction

The $K_2SiSi_3O_9$-wadeite phase (Wd) was first synthesized by Kinomura et al. (1975) and crystallographically investigated by Swanson and Prewitt (1983; space group $P6_3/m$). As part of the breakdown product of the orthoclase composition ($KAlSi_3O_8$) at high pressures (P), the Wd phase was shown to coexist with kyanite and coesite/stishovite in the P range of about 5–10 GPa (Urakawa et al. 1994; Yagi et al. 1994; Akaogi et al. 2004; Yong et al. 2006; Liu et al. 2010; Chang et al. 2013). For other compositions such as the K-amphibole ($K_2CaMg_5Si_8O_{22}(OH)_2$) and K-richterite ($KNaCaMg_5Si_8O_{22}(OH)_2$), the Wd phase was demonstrated to be a stable phase at pressures higher than 10 GPa (Inoue et al. 1998; Trønnes 2002). As proposed by Kinomura et al. (1975), therefore, the Wd phase is a potential phase which bears important geophysical implications to the subduction process of the continental crust materials (Liu et al. 2012). To thermodynamically discuss the stability of the Wd phase, its thorough and accurate knowledge on the thermochemical properties are needed.

The Wd phase has a special crystal structure (Fig. 1), with one quarter of the Si atoms in 6-coordination (Si^{VI}) and the rest three quarters in 4-coordination (Si^{IV}; Kinomura et al. 1975): The parallel layers of the three-membered rings

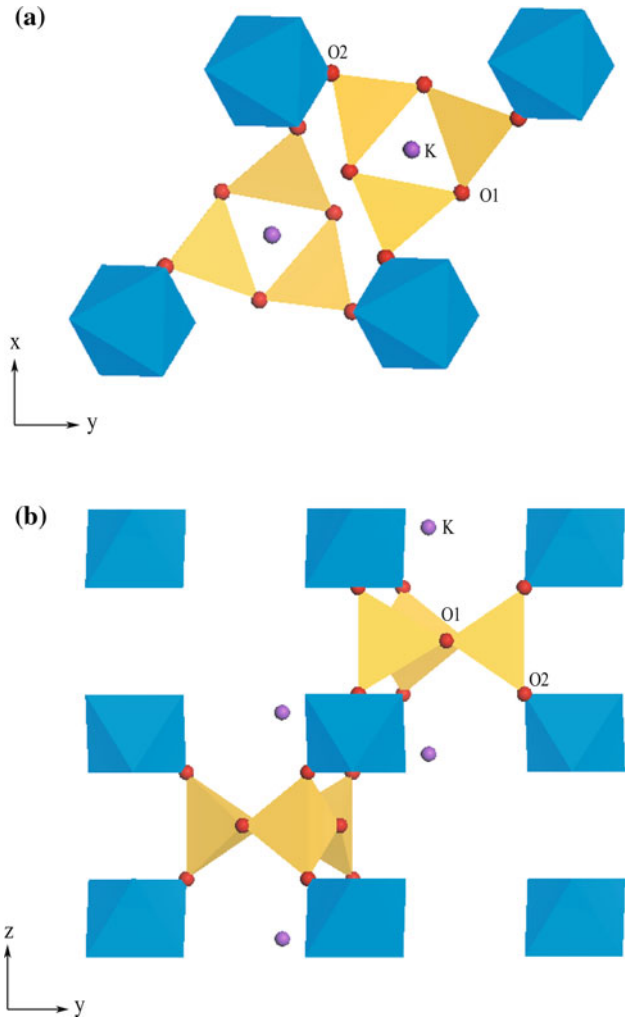

Fig. 1 Crystal structure of the Wd phase ($P6_3/m$) viewed down the [001] zone axis (**a**) and [110] zone axis (**b**). Atoms Si^{IV} and Si^{VI} locate in the tetrahedra (*yellow*) and octahedra (*blue*), respectively. O1 is bonded to two Si^{IV} and two K atoms whereas O2 bonded to one Si^{IV}, one Si^{VI} and two K atoms. *Note* the Si_3O_9 ring made of three SiO_4 tetrahedra by sharing O1. Crystallographic data were from Swanson and Prewitt (1983). To facilitate later discussion, a Cartesian coordinate system (x, y and z) has been defined, with the coordinates of x and y locating in the ring plane and the coordinate z normal to the ring plane

(Si_3O_9) of the SiO_4 tetrahedra arrange in an ABAB… stacking sequence along [001] to form the framework structure, the octahedrally coordinated Si atoms serve as bridges to link the rings, and the large K atoms occupy the cages between the layers of the rings (Swanson and Prewitt 1983). Using infrared and Raman spectroscopy, Geisinger et al. (1987) investigated the vibrational features of the Wd phase and found that it was difficult to assign the vibrational modes to the motions of any specific structure units. With the Kieffer's lattice vibrational model (Kieffer 1979a, b, c, 1980), they went further to estimate the isobaric heat capacity (C_P) and vibrational entropy at standard pressure (S^0_{298}), which unfortunately were not in any good agreement with later differential scanning calorimetry measurement (Fasshauer et al. 1998) or thermal relaxation measurement (Yong et al. 2008): Their vibrational entropy result was about 20 % smaller than that determined by Yong et al. (2008). Geisinger et al. (1987) only considered the observed Raman and infrared peaks in constructing their vibrational density of states (VDoS). Further, they did not carry out full and accurate peak assignment to their Raman and infrared spectra. In addition, they were facing difficulty in estimating the anharmonic effect on the heat capacity since accurate thermal expansion and compression data were not available at that time. These factors eventually led to large uncertainty in the calculated heat capacity, particularly at low temperatures (T; Fasshauer et al. 1998). Recently, Chang et al. (2013) employed in situ high T/P experimental techniques to investigate the thermal expansivity and compressibility of the Wd phase. Detailed vibrational spectroscopy study is still unavailable though.

In this study, we collected Raman spectra on the Wd phase synthesized at high pressure by Chang et al. (2013) and compared them with the results obtained from our first-principles simulation. With this knowledge, full and accurate peak assignment has been done for the Raman and infrared spectra of the Wd phase, and especially, neither Raman- nor infrared-active vibrational modes have been determined. Plus the newly determined thermal expansion and compression data from Chang et al. (2013), we further revised the Kieffer's lattice vibrational model from Geisinger et al. (1987) and subsequently estimated the C_P and S^0_{298} values. On the other hand, we also used the VDoS obtained from our first-principles simulation, in conjunction with a quasi-harmonic approximation (QHA) (Born and Huang 1956; Karki et al. 2000; Tsuchiya et al. 2005) to constrain these thermodynamic properties of the Wd phase.

Computational and experimental techniques

The first-principles simulations were conducted by the CASTEP code using density functional theory (DFT) (Hohenberg and Kohn 1964; Kohn and Sham 1965) and planewave pseudopotential technique (Payne et al. 1992). The exchange–correlation interaction was treated by both the local density approximation (LDA) (Cepeley and Alder 1980; Perdew and Zunger 1981) and generalized gradient approximation (GGA) with the Perdew–Burker–Ernzerhof (PBE) functional (Perdew et al. 1996). A convergence criterion of 10^{-6} a.u. on the total energy was used in the self-consistent field (SCF) calculations. The same theoretical techniques were used in our group and found to be powerful

in studying the structure and thermodynamics of silicate minerals (e.g., Liu et al. 2006; Deng et al. 2010, 2011).

More specific to this work, a planewave basis set with a cutoff of 750 eV was used to expand the electronic wave functions, and norm-conserving pseudopotential was employed to model the ion–electron interaction (Lin et al. 1993; Lee 1995). The irreducible Brillouin zone was sampled by a 3 × 3 × 2 Monkhorst–Pack grid (Monkhorst and Pack 1976). The effects of using a larger cutoff and k point mesh on the calculated properties were found to be insignificant. The initial structure model used in our simulation was from Swanson and Prewitt (1983). The computation cell contained two $K_2SiSi_3O_9$ molecules, that is, in total 30 atoms. Without any symmetric constraint, equilibrium lattice parameters and internal coordinates were optimized by minimizing the Hellmann–Feynman force on the atoms and simultaneously matching the stress on the unit cell to the target stress.

Based on the optimized structure, the phonon dispersions and VDoS of the Wd phase were calculated by diagonalizing the dynamical matrix whose elements were obtained using density functional perturbation theory (DFPT) (Baroni et al. 2001; Refson et al. 2006). The q-vector grid spacing for interpolation was 0.03 $Å^{-1}$, which represented the average distance between the Monkhorst–Pack *q*-points used in the dynamical matrix calculations. For the vibrational frequency calculation, the tolerance on the energy convergence of the SCF cycles was set to 10^{-5} a.u. The phonon dispersions were obtained at the high symmetry points (G, A, H, K, G, M, L, H). The coordinates of these points on the surface of the Brillouin zone were G = (0 0 0), A = (0 0 ½), M = (0 ½ 0), L = (0 ½ ½), K = (⅓ ⅔ 0), H = (⅓ ⅔ ½). The vibrational frequencies at the Brillouin zone center (Γ-point) were used to compare with the Raman and infrared experimental data. The internal modes were identified by visualizing the associated atomic motions with the aid of the animation of computed vibrational modes built in the CASTEP package.

In addition, unpolarized Raman spectra were collected on polished single crystals of the Wd phase from Chang et al. (2013) with a confocal micro-Raman system (Renishaw system RM-1000) in a back-scattering geometry at ambient *P–T* condition. Raman signal was excited using the 514.5 nm wavelength of an Ar^+ ion laser operating at 20 mW. The Raman spectra in the range of 50–1,200 cm^{-1} were recorded with a counting time of 20 s, 1 accumulation, a slit of 50 μm, and a 20 × objective. The corresponding spectral resolution was 1 cm^{-1}. Four Raman analyses were performed on arbitrarily selected large crystals, and the results were much comparable. The Raman data were analyzed for the frequencies of the Raman bands with a Gauss-Lorentzian peak-fitting procedure by using the PeakFit V4.12 software (SPSS Inc.).

Result and discussion

Factor group analysis and Raman spectrum at 1 atm

Factor group analysis was performed by using the method from Fateley et al. (1972), and the results are given in Table 1, with the contributions from the atoms K, Si^{VI}, Si^{IV}, O1, and O2 listed separately. The irreducible representation of the vibrational mode symmetry for the space group $P6_3/m$ is as following:

$$\Gamma = 8A_g + 6B_g + 6E_{1g} + 8E_{2g} + 6A_u + 9B_u + 8E_{1u} + 7E_{2u}, \quad (1)$$

where A_g, B_g, A_u, and B_u are nondegenerate, and E_{1g}, E_{2g}, E_{1u}, and E_{2u} are degenerate. As expected from the centric space group of $P6_3/m$ (Swanson and Prewitt 1983), there is neither coincidence between the Raman and infrared spectra nor observable LO-TO shifting for the Raman modes of the Wd phase. Among these optic modes, 22 modes (A_g, E_{1g}, and E_{2g}) are Raman-active, 14 modes (A_u and E_{1u}) are infrared-active, and 22 modes are neither Raman- nor infrared-active. In addition, there are two acoustic modes, $1A_u$ and $1E_{1u}$. All atom types except the Si^{VI} contribute to all vibrational species; the motion of the Si^{VI} contributes to the antisymmetric modes only (Table 1).

Table 1 Irreducible representations of the Wd phase ($P6_3/m$) and contributions from different atoms

	A_g(R[a])	B_g	E_{1g}(R)	E_{2g}(R)	A_u(IR[b])	B_u	E_{1u}(IR)	E_{2u}
N_{optic}	8	6	6	8	6	9	8	7
$N_{acoustic}$	0	0	0	0	1	0	1	0
K	1	1	1	1	1	1	1	1
Si^{VI}	0	0	0	0	1	1	1	1
Ring (total)[c]	7	5	5	7	5	7	7	5
Si^{IV}	2	1	1	2	1	2	2	1
O1	2	1	1	2	1	2	2	1
O2	3	3	3	3	3	3	3	3
Ring (total)[c]	7	5	5	7	5	7	7	5
Internal ring	6	4	4	6	4	6	6	4
Ring-R	1	0	1	0	0	1	0	1
Ring-T	0	1	0	1	1	0	1	0

[a] Raman-active mode

[b] Infrared-active mode

[c] All vibrational modes dominated by the displacements of the three-membered rings comprised of atoms Si^{IV}, O1, and O2 are divided into three groups: Internal ring vibration modes (Internal ring), ring-rotation (Ring-R) vibrational modes, and ring-translation (Ring-T) vibrational modes

The most prominent feature in Table 1 is that the Si_3O_9 rings comprised of Si^{IV}, O1, and O2 make significant contribution to the vibrational spectrum of the Wd phase (48 modes in total). In contrast, the vibrational modes attributed to the K and Si^{VI} atoms are only 8 and 4, respectively. The vibrational modes related to the Si_3O_9 rings can be divided into two groups: external ring vibration modes (8) and internal ring vibration modes (40). The external ring vibration modes can be further divided into two subgroups: ring-translation modes (4) and ring-rotation modes (4). The internal ring vibration modes can also be further divided into subgroups, but the procedure is much more tricky (see later discussion).

Typical Raman spectrum at room *P–T* condition is shown in Fig. 2. In total 19 Raman peaks were observed in the 50–1,200 cm^{-1} range, with 15 of them essentially identical to the Raman peaks observed by Geisinger et al. (1987). Four weak peaks at 114, 177, 407, and 521 cm^{-1} were not observed in Geisinger et al. (1987). Among the 19 Raman peaks observed in this study, the two peaks at 938 and 1,011 cm^{-1} appear somehow asymmetrical, and both peaks could be attributed to two different vibrational modes (see later discussion). The only peak which was not detected by both studies should occur at about 731 cm^{-1}, as disclosed by our later first-principles simulation.

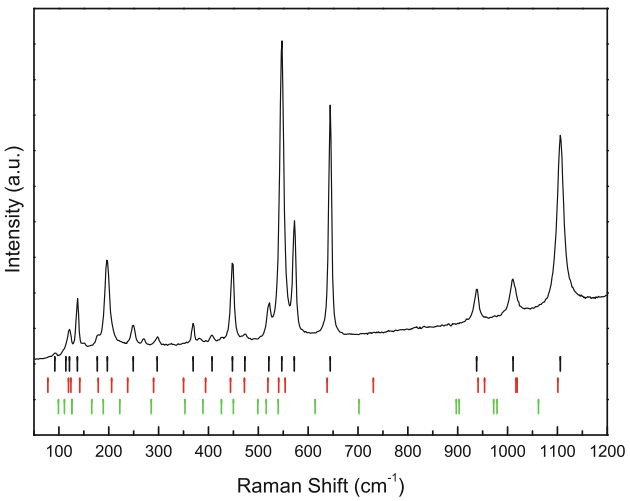

Fig. 2 Typical Raman spectrum of the Wd phase collected at ambient *P–T* condition, compared with the first-principles simulation results. Three sets of short lines below the spectrum denote the peak frequencies, with the *black lines* representing the experimental observation, the *red lines* the LDA calculation result, and the *green lines* the GGA approximation result, respectively. A few extra small peaks occasionally appeared in some of the Raman spectra and are ignored in this study. In addition, no apparent LO–TO peak splitting was observed for any of the major Raman peaks of the Wd phase

Vibrational mode calculation

The geometry parameters of the Wd phase obtained from the first-principles simulation are summarized in Table 2. Compared with the experimentally-constrained unit-cell parameters (*a*, *c* and *V*; Swanson and Prewitt 1983), the unit-cell parameters predicted by the GGA method are larger (1.21 to 3.71 %), whereas those predicted by the LDA method are smaller (1.73–3.99 %).

For the K–O bonds, the difference between the GGA result and experimental measurement (Swanson and Prewitt 1983) ranges from 0.95 to 1.33 %, whereas that between the LDA result and experimental measurement ranges from 0.86 to 3.47 %. For the Si^{VI}–O bond, the corresponding differences are 1.33 and 0.86 %, respectively. For the Si^{IV}–O bonds, the corresponding differences range from 1.11 to 1.28 %, and from 0.35 to 0.76 %, respectively. In general, the LDA result shows slightly better agreement with the experimental measurement than the GGA result.

For the two O2–Si^{VI}–O2 angels within the Si octahedra and the O1–Si^{IV}–O1 angle, O2–Si^{IV}–O2 angle, Si^{IV}–O1–Si^{IV} angle, and two O1–Si^{IV}–O2 angles in the Si_3O_9 rings, both the LDA and GGA predictions closely match the experimental measurements. For the Si^{IV}–O2–Si^{VI} angle between the octahedra and the Si_3O_9 rings, however, the difference between the GGA and experimental measurement is 0.08°, much smaller than 1.31°, the difference between the LDA prediction and experimental measurement.

The results from the vibrational mode calculation by the GGA and LDA methods for the Wd phase are listed, along with the experimental spectroscopic measurements obtained by Geisinger et al. (1987) and this work, in Table 3. The calculated Raman peak positions are compared with our experimental observations in Fig. 2. The agreement between the calculated Raman frequencies by the LDA method with the experimental measurements is good, with a maximum difference of 19 cm^{-1} (peak at about 369 cm^{-1}) and an averaged difference of 8(5) cm^{-1}. In contrast, the agreement between the calculated Raman frequencies by the GGA method with the experimental measurements is generally poor, with a maximum difference of 44 cm^{-1} (peak at about 1,106 cm^{-1}) and an averaged difference of 22(13) cm^{-1}. The distinct difference in the performance of the LDA and GGA methods is mostly due to their different accuracies in reproducing the Si^{IV}–O bonds (Table 2), which illustrates the importance of these bonds in the origins of the Raman peaks. We, therefore, only discuss the vibrational modes calculated by the LDA method hereafter.

A full assignment of the Raman-active vibrations (22 modes), which was difficult before (Geisinger et al. 1987),

Table 2 Comparison between experimental and energy-optimized crystallographic data of the Wd phase

Parameters	Experimental[a]	Calculated by the first-principles simulation			
		GGA	R. D.[b] (%)	LDA	R. D. (%)
a (Å)	6.6124 (9)	6.6925	1.21	6.4983	−1.73
c (Å)	9.5102 (8)	9.6280	1.24	9.4541	−0.59
V (Å^3)	360.11 (7)	373.46	3.71	345.74	−3.99
K-site					
K–O1	2.9758 (3)	3.011	1.18	2.936	−1.34
K–O2	2.7908 (4)	2.828	1.33	2.694	−3.47
K–O2	3.0005 (3)	3.029	0.95	2.972	−0.95
K–O1	3.2974 (2)	3.337	1.20	3.269	−0.86
Si octahedron					
Si^{VI}–O2	1.7783 (1)	1.802	1.33	1.763	−0.86
O2–Si^{VI}–O2	90.973 (8)	91.116	0.16	91.031	0.06
O2–Si^{VI}–O2	89.027 (9)	88.884	−0.16	88.969	−0.07
Si tetrahedron					
Si^{IV}–O1	1.6429 (2)	1.662	1.16	1.633	−0.60
Si^{IV}–O1	1.6596 (2)	1.678	1.11	1.647	−0.76
Si^{IV}–O2	1.5916 (1)	1.612	1.28	1.586	−0.35
O1–Si^{IV}–O1	105.553 (12)	105.780	0.22	105.953	0.38
O1–Si^{IV}–O2	103.983 (5)	103.666	−0.30	103.582	−0.39
O1–Si^{IV}–O2	111.632 (4)	111.678	0.04	111.780	0.13
O2–Si^{IV}–O2	118.579 (8)	118.831	0.21	118.635	0.05
Si^{IV}–O1–Si^{IV}	134.447 (5)	134.220	−0.17	134.047	−0.30
Si^{IV}–O2–Si^{VI}	141.760 (4)	141.644	−0.08	139.910	−1.31

[a] Swanson and Prewitt (1983)

[b] Relative difference

has been completed, with the details shown in Table 3. Of the 19 Raman peaks observed in our spectroscopic experiments, 17 peaks can be confidently related to 17 vibrational modes. The rest two asymmetrical Raman peaks, one at 938 cm^{-1} and the other at 1,011 cm^{-1}, can be explained by the overlap of the vibrational modes of A_g 954 and E_{2g} 941 cm^{-1} and the overlap of the vibrational modes of E_{1g} 1,017 cm^{-1} and E_{2g} 1,019 cm^{-1}, respectively. The only Raman-active mode, which was not detected by the experimental measurements, is the vibrational mode of E_{2g} at about 731 cm^{-1} (LDA).

A full assignment of the infrared-active vibrations (14 modes) has been completed as well, with the details shown in Table 3. The eight infrared peaks detected by our first-principles calculation and the experimental measurements (Geisinger et al. 1987) show good consistency, with only one exception, the peak at 520 cm^{-1}, which has a calculated frequency 44 cm^{-1} lower than the experimentally obtained value. The six infrared-active peaks (with five peaks occurring at frequencies lower than 400 cm^{-1}), undetected by Geisinger et al. (1987), have been assigned to specific vibrational modes, but they need further infrared spectroscopic investigation.

In addition, the 22 neither Raman-active nor infrared-active modes have also been assigned to specific vibrational modes (Table 3). The existence of this large number of inactive vibrational modes for the Wd phase has significant effect on the density distribution of the vibrational modes in the Kieffer's model, which certainly affects the isochoric heat capacity (C_V) estimate (see later discussion).

In the structure of the Wd phase, the atomic displacements include K translation, SiO_6 octahedral motion, external ring motion (ring translation and ring rotation), and internal ring motions. Due to the interplay of the different structure units, the vibrational modes are always related to the atomic displacements consisting of multiple components. Taking the E_{1g} mode at ~78 cm^{-1} as an example, it includes contributions from the ring rotation (*xy*) and the K translation (*xy*). The eight K translation-dominant vibrational modes, as predicted by the factor group analysis (Table 1), appear at low frequencies (from ~107 to 142 cm^{-1}; Table 3). The four SiO_6 octahedron motion-dominant modes (Table 1) have the frequencies of ~442, 476, 569, and 643 cm^{-1} (Table 3). The external ring motion-dominant modes also appear at low frequencies: the four ring-rotation-dominant vibrational modes and four ring-translation-dominant modes occur at low frequencies, from ~78 to 261, and up to 179 cm^{-1}, respectively. The internal ring motions include the Si^{IV}–O1

Table 3 Lattice vibrational modes (in cm^{-1}) from the first-principles simulation for the Wd phase

Mode no.	Experimental		Calculated		Symmetry	Mode assignment[a]
			LDA	GGA		
Q1			0[b]	0[b]	A_u (acoustic)	Ring-T (*z*) + K-T (*z*) + SiO_6-T (*z*)
Q2			0	0	E_{1u} (acoustic)	Ring-T (*xy*) + K-T (*xy*) + SiO_6-T (*xy*)
Q3	92[b]	95[c]	78	99	E_{1g} (R)	Ring-R (*xy*) + K-T (*xy*)
Q4			107	105	B_g	K-T (*z*)
Q5			110	97	E_{2u}	K-T (*xy*)
Q6	114		119	111	E_{2g} (R)	K-T (*xy*) + Ring-T (*xy*)
Q7			122	119	A_u (IR)	K-T (*z*) + Ring-T (*z*) + SiO_6-T (*z*)
Q8	121	123	124	126	A_g (R)	K-T (*z*)
Q9			135	118	E_{1u} (IR)	K-T (*xy*) + Ring-T (*xy*) + SiO_6-T (*xy*)
Q10			138	137	B_u	K-T (*z*)
Q11	137	138	142	126	E_{1g} (R)	K-T (*xy*) + Ring-R (*xy*)
Q12			146	145	B_g	Ring-T (*z*) + K-T (*z*)
Q13	177		179	166	E_{2g} (R)	Ring-T (*xy*) + K-T (*xy*)
Q14			187	190	E_{2u}	Ring-R (*xy*) + K-T (*xy*) + SiO_6-T (*xy*)
Q15	197	198	206	189	A_g (R)	Ring-R (*z*) + K-T (*z*)
Q16	249	249	238	222	E_{1g} (R)	ν19[d] + ν1
Q17			244	227	E_{2u}	ν19 + ν1 + SiO_6-T (*xy*)
Q18			246	241	A_u (IR)	ν2 + Ring-T (*z*) + SiO_6-T (*z*)
Q19			255	251	E_{1u} (IR)	ν3 + ν14 + SiO_6-T (*xy*)
Q20			261	249	B_u	Ring-R (*z*) + K-T (*z*) + SiO_6-T (*z*)
Q21	297	300	290	285	E_{2g} (R)	ν3 + ν14
Q22			296	289	E_{2u}	ν4 + ν19 + SiO_6-D (*xy*)
Q23			320	305	B_g	ν2 + Ring-T (*z*)
Q24	369	370	350	353	A_g (R)	ν3 + Ring-R (*z*)
Q25			363	363	B_u	ν3 + Ring-R (*z*) + SiO_6-D (*z*)
Q26	407		394	389	E_{2g} (R)	ν3 + ν14
Q27			398	393	E_{1u} (IR)	ν3 + ν14
Q28		403	404	377	A_u (IR)	ν1 + ν13 + SiO_6-D (*z*)
Q29			415	395	B_g	ν2 + ν13
Q30		440	427	413	E_{1u} (IR)	ν3 + ν15 + SiO_6-D (*xy*)
Q31			442	427	B_u	SiO_6-D (*z*) + ν6
Q32	448	449	444	426	E_{1g} (R)	ν1 + ν19
Q33			456	437	E_{2u}	ν1 + ν19 + SiO_6-D (*xy*)
Q34	473	476	472	450	E_{2g} (R)	ν3 + ν15
Q35		520	476	456	A_u (IR)	SiO_6-D (*z*) + ν2
Q36		521	519	499	E_{1g} (R)	ν1 + ν19
Q37	547	548	541	516	A_g (R)	ν3 + ν8
Q38			541	516	B_u	ν3 + ν8
Q39	572	573	554	540	A_g (R)	ν9 + ν3
Q40			567	548	B_u	ν9 + ν3
Q41		570	569	532	E_{1u} (IR)	SiO_6-D (*xy*) + ν3
Q42			618	591	B_g	ν1 + ν13
Q43	644	645	638	614	A_g (R)	ν10 + ν5
Q44			643	600	E_{2u}	SiO_6-D (*xy*) + ν1 + ν19
Q45		652	658	615	A_u (IR)	ν1 + ν13 + SiO_6-D (*z*)
Q46			713	679	B_u	ν10 + ν5 + SiO_6-D (*z*)
Q47			731	702	E_{2g} (R)	ν16 + ν3

Table 3 continued

Mode no.	Experimental		Calculated		Symmetry	Mode assignment[a]
			LDA	GGA		
Q48		746	741	708	E_{1u} (IR)	ν16 + ν3 + SiO_6-D (*xy*)
Q49	938	939	941	897	E_{2g} (R)	ν6 + ν17
Q50			952	901	B_u	ν11 + ν6
Q51	938	939	954	903	A_g (R)	ν11 + ν6
Q52		988	989	944	E_{1u} (IR)	ν6 + ν17
Q53	1,011	1,012	1,017	972	E_{1g} (R)	ν7
Q54	1,011	1,012	1,019	979	E_{2g} (R)	ν18 + ν6
Q55			1,032	991	E_{1u} (IR)	ν18 + ν6
Q56		1,035	1,039	998	A_u (IR)	ν7
Q57			1,054	1,013	B_u	ν6 + ν12
Q58			1,072	1,029	E_{2u}	ν7
Q59	1,106	1,108	1,101	1,062	A_g (R)	ν6 + ν12
Q60			1,203	1,160	B_g	ν7

[a] Displacements arranged in the order of magnitude. *T* translation, *R* rotation, *D* deformation. (*z*) after T or D means the translation or deformation generally parallel to the *z*-coordinate whereas (*xy*) after T or D means the translation or deformation mostly occurring in the *xy* plane (orientation of the *x*, *y* and *z* shown in Fig. 1). (*z*) after R means the rotating axis generally parallel to the *z*-coordinate whereas (*xy*) after R means the rotating axis almost confined in the *xy* plane

[b] This work. Our results suggest that no LO-TO shifting for the Raman modes exists, and no significant LO–TO shifting for the infrared modes appears

[c] Geisinger et al. (1987)

[d] Components used to describe the vibrational modes of the C_{3h}-symmetry Si_3O_9 rings (ν1–ν19) are sketched in Figs. 3 and 4

displacement and Si^{IV}–O2 displacement and dominate the rest 40 vibrational modes which can be attributed to the O1 atoms (12 modes), O2 atoms (24 modes), and Si^{IV} atoms (4 modes; Table 1). Considering the lengths of the Si^{IV}–O1 and Si^{IV}–O2 bonds (Table 2) and the relative magnitudes of the Si^{IV}–O1 displacement and Si^{IV}–O2 displacement, the four modes attributed to the Si^{IV} atoms are mostly Si^{IV}–O2 displacement-dominant, which leads to 28 Si^{IV}–O2 displacement-dominant modes and 12 Si^{IV}–O1 displacement-dominant modes (Table 3). To describe the internal ring motions of the O1, O2, and Si^{IV} atoms, we have defined two labeling schemes, with the first for the Si^{IV}–O2 displacements (ν1 through ν7; Fig. 3) and the second for the Si^{IV}-O1 displacements (ν8 through ν19; Fig. 4).

In the Raman spectrum of the Wd phase there are three major peaks locating at about 547, 572 and 644 cm^{-1} (Fig. 2). They are all A_g modes caused by the internal ring motions and have nothing to do with the SiO_6 octahedral group (Table 3). These peaks were previously ascribed to an origin either from the symmetric stretching of the SiO_6 octahedra or from the internal ring motions (Geisinger et al. 1987). On the other hand, the motion of the SiO_6 groups was tentatively regarded as the contributor to the strong infrared band at 746 cm^{-1} by Geisinger et al. (1987). Our analysis has shown that this infrared peak indeed contains some contribution from the motion of the SiO_6 octahedra, but also contains significant contribution from the internal ring motions.

Heat capacity calculation

The isochoric heat capacity of the Wd phase has been calculated by using two methods. Firstly, the phonon dispersions and VDoS of the Wd phase were calculated by the first-principles method using density functional perturbation theory. The dynamical matrices were computed at 24 wave (q) vectors in the Brillouin zone of the primitive cell of the Wd phase. We then interpolated the dynamical matrices to obtain the bulk phonon dispersions. The predicted dispersion curves along several symmetry directions and the VDoS are shown in Fig. 5. The results of the phonon spectra were used to compute the internal energy (*E*) and isochoric heat capacity as functions of temperature. The temperature dependence of the *E* was given by:

$$E(T) = E_{\text{tot}} + E_{\text{ZP}} + \int \frac{h\omega}{\exp\left(\frac{h\omega}{kT}\right) - 1} F(\omega)\mathrm{d}\omega, \quad (2)$$

where E_{tot} was the total electronic energy at 0 K, E_{ZP} the zero point vibrational energy, *h* the Planck's constant, *k* the Boltzmann's constant, and $F(\omega)$ the vibrational density of states. E_{ZP} was evaluated as:

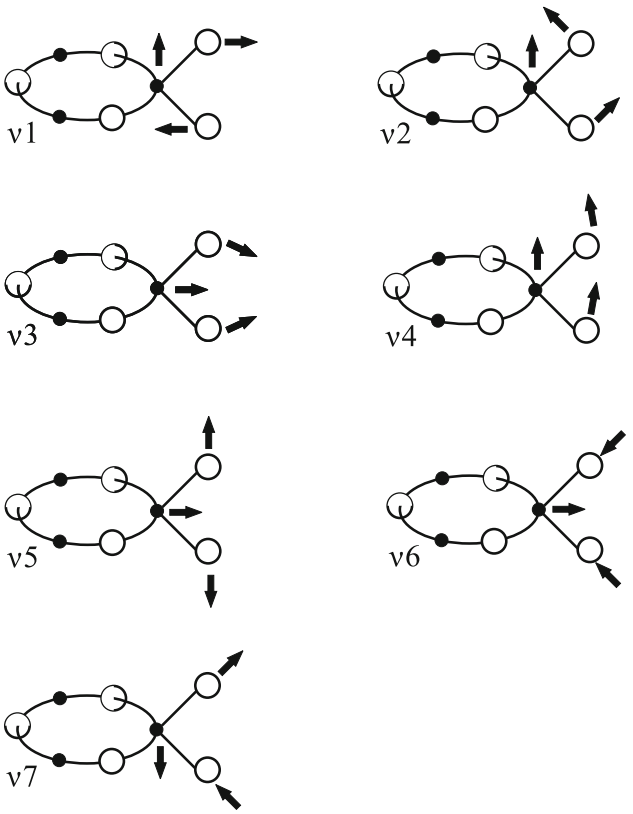

Fig. 3 Labeling scheme for the Si^{IV}–O2 displacements (viewed along the [001] zone axis with some tilting to show the ring). Small *filled circles* stand for the Si^{IV} atoms, whereas large empty circles for the O atoms (O1 and O2). For clarity, every sketch shows one pair of O2 atoms only, and the remaining Si-O2 displacements around the ring can be generated by the symmetry operation (C_{3h}). *Arrow* is drawn to show the direction of the motion of the atom in the normal mode only

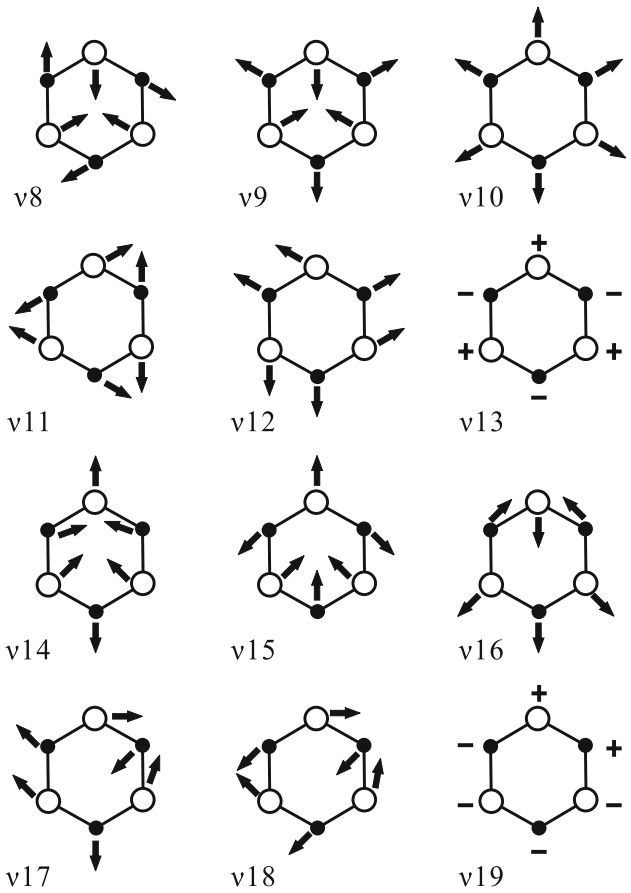

Fig. 4 Labeling scheme for the Si^{IV}–O1 displacements (viewed down the [001] zone axis). *Small filled circles* represent the Si^{IV} atoms, whereas large empty circles the O1 atoms. *Arrow* is drawn to show the direction of the motion of the atom in the normal mode only. *Plus* and *minus* indicate the atomic displacements above and below the ring plane

$$E_{ZP} = \frac{1}{2}\int F(\omega)h\omega \mathrm{d}\omega. \quad (3)$$

The lattice contribution to the C_V was given by:

$$C_V(T) = k\int \frac{\left(\frac{h\omega}{kT}\right)^2 \exp\left(\frac{h\omega}{kT}\right)}{\left[\left(\frac{h\omega}{kT}\right)^2 - 1\right]^2} F(\omega)\mathrm{d}\omega. \quad (4)$$

The result of the C_V calculated by this method, which contained a component of the first-principles simulation, is shown in Table 4.

Secondly, the C_V of the Wd phase was calculated by the Kieffer's lattice vibrational model (Kieffer 1979a, b, c), as Geisinger et al. (1987) did before. Using rather simplified density state for phonon dispersion, the Kieffer's model is a convenient and comparable method to the calorimetric measurement in estimating the heat capacity of certain substances (Kojitani et al. 2012, 2013). Due to the unavailability of the data about the Raman-inactive and infrared-inactive vibrational modes and the data of the infrared-active vibrational modes at frequencies below 400 cm^{-1}, the Kieffer's model used by Geisinger et al. was simplified to include two optic continua only, with the first extending from 95 to 746 cm^{-1} and the second from 939 to 1,110 cm^{-1}. In this study, our first-principles simulation provided all these once unavailable data, so that the density distribution of the vibrational modes was rigorously assessed, which led to a more appropriate Kieffer's model. The details of our model and related physical properties have been tabulated in Table 5 and schematically illustrated in Fig. 6. In our model, there were four optic continua, ranging from 92 to 150 cm^{-1}, from 150 to 300 cm^{-1}, from 300 to 750 cm^{-1}, and from 938 to 1,200 cm^{-1}, These four optic continua, from low frequency to high frequency, contained 15, 17, 37 and 18 vibrational modes, respectively. The frequency range from 750 to 938 cm^{-1} contained no vibrational mode, so that it was regarded as a stopping band, as clearly shown by the

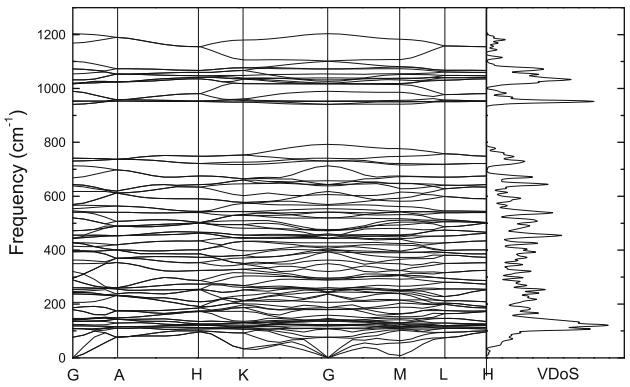

Fig. 5 Phonon dispersions and VDoS of the Wd phase (LDA)

phonon dispersions in Fig. 5. The result of the C_V calculated by this method is shown in Table 4 as well.

Table 4 shows that our C_V values obtained by using these two methods are in good agreement for all temperatures, with an averaged different of 2.0(8) J mol^{-1} K^{-1}. In contrast, the C_V values obtained by our Kieffer's model and that in Geisinger et al. (1987) are very different, with an averaged difference of 9.8(95) J mol^{-1} K^{-1}. More specifically, this difference is negatively correlated to temperature, being as large as 30 J mol^{-1} K^{-1} at 100 K and gradually reduced to negligible 2.2 J mol^{-1} K^{-1} at 800 K.

Isobaric heat capacity (C_P) was calculated by adding an anharmonic effect to the C_V obtained from the calculations done above, using the following equation:

$$C_P = C_V + \alpha_T^2 K_{0,T} V_T T, \quad (5)$$

where α_T, $K_{0,T}$, and V_T were the thermal expansivity, isothermal bulk modulus, and volume at 1 atm and T K, respectively. For the Wd phase, $\alpha_T = 2.47(21) \times 10^{-5} + 1.45(36) \times 10^{-8}\, T$ (Chang et al. 2013). The room-T equation of state of the Wd phase was recently

Table 4 Results of heat capacity calculations of the Wd phase, compared with those by calorimetric measurements

T (K)	Calculated by first-principles[a]		T (K)	Calculated by Kieffer's model[a]		T (K)	Calculated by Kieffer's model[b]		T (K)	Experimental
	C_V (J mol^{-1} K^{-1})	C_P (J mol^{-1} K^{-1})		C_V (J mol^{-1} K^{-1})	C_P (J mol^{-1} K^{-1})		C_V (J mol^{-1} K^{-1})	C_P (J mol^{-1} K^{-1})		C_P (J mol^{-1} K^{-1})
51	38.9	39.2 (1)[c]	50	39.8	40.1 (1)	50	23.7	24.1	50	40.98 (27)[d]
101	98.7	99.4 (1)	100	101.2	102.0 (1)	100	71.2	72.1	100	101.60 (45)[d]
152	147.1	148.3 (1)	150	148.1	149.3 (1)	150	118.7	119.9	156	155.13 (54)[d]
202	186.7	188.4 (1)	200	186.0	187.6 (1)	200	161.2	162.9	202	191.72 (77)[d]
253	218.9	221.0 (1)	250	217.0	219.1 (1)	250	197.3	199.4	242	219.89 (70)[d]
303	245.0	247.7 (2)	300	242.3	245.0 (2)	300	227.0	229.5	300	248.56 (100)[e]
354	266.1	269.4 (3)	350	263.1	266.3 (3)	350	251.1	254.1	353	267.98 (100)[e]
404	283.1	287.1 (5)	400	280.0	283.9 (5)	400	270.6	274.0	403	282.92 (100)[e]
455	296.9	301.5 (7)	450	293.8	298.5 (6)	450	286.3	290.2	453	292.82 (100)[e]
505	308.0	313.5 (9)	500	305.1	310.5 (9)	500	299.1	303.3	498	310.15 (0)[e]
556	317.1	323.4 (12)	550	314.4	320.6 (11)	550	309.4	314.1	553	312.07 (100)[e]
606	324.5	331.7 (15)	600	322.0	329.2 (15)	600	317.9	323.1	598	325.26 (0)[e]
657	330.7	338.8 (20)	650	328.4	336.5 (19)	650	325.0	330.5		
707	335.9	344.9 (25)	700	333.7	342.8 (24)	700	330.8	336.8		
758	340.2	350.3 (31)	750	338.2	348.4 (30)	750	335.7	342.2		
808	343.8	355.1 (38)	800	342.1	353.3 (37)	800	339.9	346.7		
859	346.9	359.4 (46)	850	345.3	357.8 (45)	850	343.4	350.7		
909	349.6	363.3 (56)	900	348.1	361.9 (54)	900	346.4	354.2		
950	351.5	366.3 (65)	950	350.6	365.7 (65)	950	349.0	357.3		
1,000	353.6	369.7 (78)	1,000	352.7	369.2 (78)	1,000	351.3	360.0		

[a] This work. Two methods used in the calculation: one containing the component of the first-principles calculation and the other employing the Kieffer's model. For both methods, experimentally determined thermal expansion coefficient and isothermal bulk modulus of the Wd phase were involved (Eq. 5)

[b] Geisinger et al. (1987)

[c] The number in the parentheses represents one standard deviation in the rightmost digit

[d] Yong et al. (2008)

[e] Fasshauer et al. (1998)

Table 5 Parameters of the new Kieffer's model and physical properties of the Wd phase used in the heat capacity calculation

	Lower limit (cm^{-1})	Upper limit (cm^{-1})	Number of modes
TA1	0	70[a]	1
TA2	0	76[a]	1
LA	0	122[a]	1
OC1	92	150	15
OC2	150	300	17
OC3	300	750	37
OC4	938	1,200	18
Formula weight (g/mol)	334.56		
V_{298} (cm^3/mol)	108.432[b]		
Z	2[b]		
$K_{0,298}$ (GPa)	97 (3)[c]		
$(\partial K_{P,T}/\partial P)_T$	4[c]		
$(\partial K_{P,T}/\partial T)_P$	0		
$\alpha_T = a_0 + a_1 T$ (T in K)			
$a_0 \times 10^5$	2.47 (21)[c]		
$a_1 \times 10^8$	1.45 (36)[c]		

TA transverse acoustic mode, *LA* longitudinal acoustic mode, *OC* optic continuum

[a] Geisinger et al. (1987)

[b] Swanson and Prewitt (1983)

[c] Chang et al. (2013)

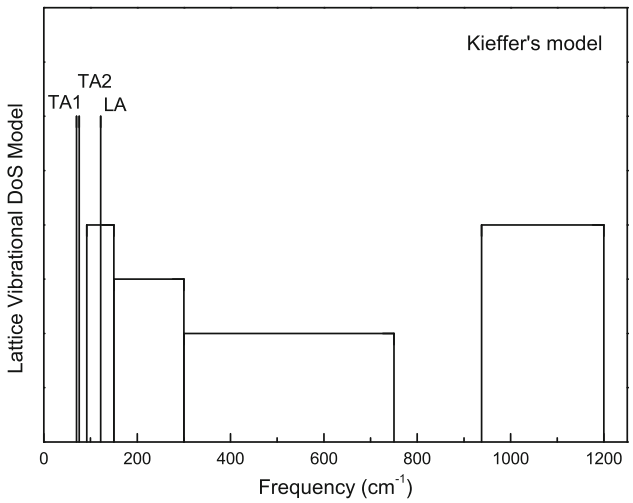

Fig. 6 Updated Kieffer's lattice vibrational model for the Wd phase. Boxes represent the optic continua. *Vertical lines* show the cutoff frequencies of the transversal acoustic modes (TA) and longitudinal acoustic modes (LA; Geisinger et al. 1987)

measured by Chang et al. (2013), attaining $K_{0,298} = 97(3)$ GPa (its first pressure derivative fixed as 4). The temperature derivative of $K_{0,T}$ has not been experimentally determined, thus assumed as zero in our calculation ($K_{0,T} = K_{0,298}$). V_T at T K was calculated with the following equation:

$$V_T = V_{298} \exp\left(\int_{298}^{T} \alpha_T \mathrm{d}T\right), \quad (6)$$

where $V_{298} = 108.432$ cm^3/mol (Swanson and Prewitt 1983). The calculated C_P values are listed in Table 4, along with the results from Geisinger et al. (1987), from Fasshauer et al. (1998) and from Yong et al. (2008). Errors of our C_P values were propagated from the uncertainty in the thermal expansion coefficients and were estimated to be ~0.2–2.1 %, increasing with rising temperature. The calculated C_P data were then expressed using the following polynomial of temperature (Berman and Brown 1985; T range 298–1,500 K),

$$C_P = k_1 + k_2 T^{-0.5} + k_3 T^{-2} + k_4 T^{-3}, \quad (7)$$

where C_P was in J $mol^{-1}K^{-1}$ and T in K. The arrived fitting coefficients are tabulated in Table 6.

Our calculated C_P values are compared in Fig. 7 with the calorimetric data measured by Fasshauer et al. (1998) and Yong et al. (2008), and with the estimate using the Kieffer's lattice vibrational model by Geisinger et al. (1987). For the T range of 5–303 K, our C_P data show excellent agreement with those measured by using the Physical Properties Measurement System (Yong et al. 2008). For the T range of 195 to 598 K, our C_P data are in good agreement with those measured by using the differential scanning calorimeter (Fasshauer et al. 1998). Since the Wd phase is not stable at T above 873 K (Swanson 1986; room P), it is not possible to make direct calorimetric measurement at higher T. The excellent agreement between our calculated C_P and the direct calorimetric measurements at relatively low T verifies our calculating methods, which provides us a potential tool to explore the C_P values at relatively high T. What should be kept in mind is the uncertainty in the extrapolation of the thermal expansion data to higher T. The C_P data calculated from the two Kieffer's lattice vibrational models are significantly different in the whole T range. This discrepancy was mainly caused by the difference in the Kieffer's models, as outlined before. Other factors included the different thermal expansion data and compression data which were used in the conversions from C_V to C_P (for more details, see Chang et al. 2013).

Entropy calculation

The obtained C_P values have been applied to the calculation of the vibrational entropy at T K using the following equation

Table 6 Fitting parameters for the C_P data of the Wd phase[a]

Data source	$k_1 \times 10^{-2}$	$k_2 \times 10^{-3}$	$k_3 \times 10^{-6}$	$k_4 \times 10^{-9}$
This study (first-principles)[b]	4.694 (6)	−2.90 (2)	−9.5 (2)	1.36 (3)
This study (Kieffer's model)[b]	4.759 (6)	−3.15 (2)	−8.8 (2)	1.31 (3)
Fasshauer et al. (1998)[c]	4.991 (19)	−4.35 (3)	–	–

[a] Parameters have been obtained by a least squares fitting to the C_P data

[b] Valid T range is from 298 to 1,000 K. The C_p data used in the fitting were derived by using the C_v results obtained with either the first-principles method or the Kieffer's model, plus the experimental results such as the thermal expansion coefficient, and isothermal bulk modulus of the Wd phase (Eq. 5)

[c] Calorimetric measurement for the T range from 195 to 598 K

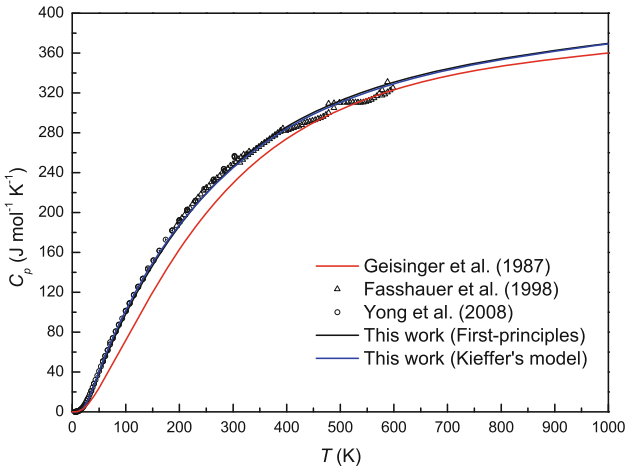

Fig. 7 Isobaric heat capacity of the Wd phase. Our C_v results from two different calculating methods, the first-principles method and the Kieffer's model, were combined with the experimental results of thermal expansion coefficient and isothermal bulk modulus of the Wd phase to derive the C_p values (Eq. 5)

$$S_T^0 = \int_0^T \frac{C_P}{T} \mathrm{d}T. \quad (8)$$

The vibrational entropies at 298 K (S_{298}^0) obtained by the present and previous studies are compared in Table 7. In this work, the S_{298}^0 was calculated to be 249.5(40) J mol^{-1} K^{-1} by the Kieffer's lattice vibrational model method and to be 250.4 J mol^{-1} K^{-1} by the method containing the component of the first-principles simulation. Our results not only show good internal consistency, but also agree well with the calorimetric result obtained by Yong et al. (2008). In contrast, these values are significantly larger than the estimated value of 232(10) J mol^{-1} K^{-1} based on an internally consistent thermodynamic database by Fasshauer et al. (1998), suggesting that some of the thermodynamic data in their database still need further evaluation and refinement (Chang et al. 2013). Finally, these values are substantially larger than the S_{298}^0 determined by Geisinger et al. (1987), and the reasons to this discrepancy have been fully explained by the preceding discussion.

Table 7 S_{298}^0 of the Wd phase

Data source	S_{298}^0 (J mol^{-1} K^{-1})	Method
This study	250.4	First-principles calculation[a]
This study	249.5 (40)	Kieffer's model[a]
Yong et al. (2008)	253.8 (6)	Calorimetric measurement
Fasshauer et al. (1998)	232 (10)	Thermodynamic estimate
Geisinger et al. (1987)	198.9 (40)	Kieffer's model

[a] The C_p data, used to calculate the S_{298}^0, were derived by using the C_v results obtained with either the first-principles method or the Kieffer's model and experimental results such as the thermal expansion coefficient and isothermal bulk modulus of the Wd phase (Eq. 5)

Acknowledgments We thank two anonymous reviewers for their constructive suggestions, and also thank Dr T. Tsuchiya for his comments on and editorial help to our paper. This investigation was financially supported by the National Natural Science Foundation of China (Grants No. 41090371 and 41174071) and the State Key Laboratory of Ore Deposit Geochemistry, Institute of Geochemistry, Chinese Academy of Sciences (Grant No. 201114).

References

Akaogi M, Kamii N, Kishi A, Kojitani H (2004) Calorimetric study on high-pressure transitions in $KAlSi_3O_8$. Phys Chem Mineral 31:85–91

Baroni S, de Gironcoli S, Dal Corso A, Giannozzi P (2001) Phonons and related crystal properties from density-functional perturbation theory. Rev Mod Phys 73:515–562

Berman RG, Brown TH (1985) Heat capacity of minerals in the system Na_2O–K_2O–CaO–MgO–FeO–Fe_2O_3–Al_2O_3–SiO_2–TiO_2–H_2O–CO_2: representation, estimation, and high-temperature extrapolation. Contrib Mineral Petrol 89:168–183

Born M, Huang K (1956) Dynamical theory of crystal lattices (international series of monographs on physics). Clarendon Press, Oxford, p 420

Cepeley DM, Alder BJ (1980) Ground state of the electron gas by a stochastic method. Phys Rev Lett 45:566–569

Chang L, Chen Z, Liu X, Wang H (2013) Expansivity and compressibility of wadeite-type $K_2Si_4O_9$ determined by in situ high T/P experiments, and their implication. Phys Chem Mineral 40:29–40

Deng L, Liu X, Liu H, Dong J (2010) High-pressure phase relations in the composition of albite $NaAlSi_3O_8$ constrained by an ab initio and quasi-harmonic Debye model, and their implications. Earth Planet Sci Lett 298:427–433

Deng L, Liu X, Liu H, Zhang Y (2011) A first-principles study of the phase transition from Holl-I to Holl-II in the composition $KAlSi_3O_8$. Am Mineral 96:974–982

Fasshauer DW, Wunder B, Chatterjee ND, Höhne GWH (1998) Heat capacity of wadeite-type $K_2Si_4O_9$ and the pressure-induced stable decomposition of K-feldspar. Contrib Mineral Petrol 131:210–218

Fateley WG, Dollish FR, McDevitt NT, Bentley FF (1972) Infrared and Raman selection rules for molecular and lattice vibration: the correlation method. Wiley Interscience, New York, p 222

Geisinger KL, Ross NL, McMillan P, Navrotsky A (1987) $K_2Si_4O_9$: energetics and vibrational spectra of glass, sheet silicate, and wadeite-type phases. Am Mineral 72:984–994

Hohenberg P, Kohn W (1964) Inhomogeneous electron gas. Phys Rev 136:864–871

Inoue T, Irifune T, Yurimoto H, Miyagi I (1998) Decomposition of K-amphibole at high pressures and implications for subduction zone volcanism. Phys Earth Planet Inter 107:221–231

Karki BB, Wentzcovitch RM, de Gironcoli S, Baroni S (2000) Ab initio lattice dynamics of $MgSiO_3$ perovskite at high pressure. Phys Rev B 62:14750–14756

Kieffer SW (1979a) Thermodynamics and lattice vibrations of minerals: 1. Mineral heat capacities and their relationships to simple lattice vibrational modes. Rev Geophys Space Phys 17:1–19

Kieffer SW (1979b) Thermodynamics and lattice vibrations of minerals: 2. Vibrational characteristics of silicates. Rev Geophys Space Phys 17:20–34

Kieffer SW (1979c) Thermodynamics and lattice vibrations of minerals: 3. Lattice dynamics and an approximation for minerals with application to simple substances and framework silicates. Rev Geophys Space Phys 17:35–59

Kieffer SW (1980) Thermodynamics and lattice vibrations of minerals: 4. Application to chain and sheet silicates and orthosilicates. Rev Geophys Space Phys 18:862–886

Kinomura N, Kume S, Koizumi M (1975) Synthesis of $K_2SiSi_3O_9$ with silicon in 4- and 6-coordination. Mineral Mag 40:401–404

Kohn W, Sham LJ (1965) Self-consistent equations including exchange and correlation effects. Phys Rev 140:1133–1138

Kojitani H, Oohata M, Inoue T, Akaogi M (2012) Redetermination of high-temperature heat capacity of Mg_2SiO_4 ringwoodite: measurement and lattice vibrational model calculation. Am Mineral 97:1314–1319

Kojitani H, Többens DM, Akaogi M (2013) High-pressure Raman spectroscopy, vibrational mode calculation, and heat capacity calculation of calcium ferrite-type $MgAl_2O_4$ and $CaAl_2O_4$. Am Mineral 98:197–206

Lee MH (1995) Advanced pseudopotentials for large scale electronic structure calculations, PhD thesis. University of Cambridge

Lin JS, Qteish A, Payne MC, Heine V (1993) Optimized and transferable nonlocal separable ab initio pseudopotentials. Phys Rev B 47:4174–4180

Liu H, Zhao J, Ji G, Wei D, Gong Z (2006) Vibrational properties of molecule and crystal of TATB: a comparative density functional study. Phys Lett A 358:63–69

Liu X, Hu Z, Deng L (2010) Feldspars under conditions of high temperature-high pressure. Acta Petrol Sin 26:3641–3650

Liu X, Ohfuji H, Nishiyama N, He Q, Sanehira T, Irifune T (2012) High-P behavior of anorthite composition and some phase relations of the $CaO–Al_2O_3–SiO_2$ system to the lower mantle of the Earth, and their geophysical implications. J Geophys Res 117:B09205

Monkhorst HJ, Pack JD (1976) Special points for Brillouin-zone integrations. Phys Rev B 13:5188–5192

Payne MC, Teter MP, Allan DC, Arias TA, Joannopoulos JD (1992) Iterative minimization techniques for ab initio total-energy calculations: molecular dynamics and conjugate gradients. Rev Mod Phys 64:1045–1097

Perdew JP, Zunger A (1981) Self-interaction correction to density-functional approximations for many-electron systems. Phys Rev B 23:5048–5079

Perdew JP, Burke K, Ernzerhof M (1996) Generalized gradient approximation made simple. Phys Rev Lett 77:3865–3868

Refson K, Tulip PR, Clark SJ (2006) Variational density-functional perturbation theory for dielectrics and lattice dynamics. Phys Rev B 73:155114

Swanson DK, Prewitt CT (1983) The crystal structure of $K_2Si^{VI}Si_3^{IV}O_9$. Am Mineral 68:581–585

Trønnes RG (2002) Stability range and decomposition of potassic richterite and phlogopite end members at 5–15 GPa. Mineral Petrol 74:129–148

Tsuchiya J, Tsuchiya T, Wentzcovitch RM (2005) Vibrational and thermodynamic properties of $MgSiO_3$ postperovskite. J Geophys Res 110:B02204

Urakawa S, Kondo T, Igawa N, Shimomura O, Ohno H (1994) Synchrotron radiation study on the high-pressure and high-temperature phase relations of $KAlSi_3O_8$. Phys Chem Mineral 21:387–391

Yagi A, Suzuki T, Akaogi M (1994) High pressure transitions in the system $KAlSi_3O_8–NaAlSi_3O_8$. Phys Chem Mineral 21:12–17

Yong W, Dachs E, Withers AC, Essene EJ (2006) Heat capacity and phase equilibria of hollandite polymorph of $KAlSi_3O_8$. Phys Chem Mineral 33:167–177

Yong W, Dachs E, Withers AC, Essene EJ (2008) Heat capacity and phase equilibria of wadeite-type $K_2Si_4O_9$. Contrib Mineral Petrol 155:137–146